Peptide Secondary Structure Determination by Three-Pulse Coherent Vibrational Spectroscopies: A Simulation Study

Darius Abramavicius, Wei Zhuang, and Shaul Mukamel*

Chemistry Department, University of California, Irvine, California 92697-2025

Received: May 26, 2004; In Final Form: July 21, 2004

Amide I mode vibrational spectra of four ideal secondary structural motiffs of peptides, α helix, 3_{10} helix, parallel β sheet, and antiparallel β sheet, in response to three infrared pulses with wavevectors $\mathbf{k}_1$, $\mathbf{k}_2$, and $\mathbf{k}_3$ are simulated using a vibrational exciton model. Correlation plots of the signals generated at $-\mathbf{k}_1 + \mathbf{k}_2 + \mathbf{k}_3$ and $+\mathbf{k}_1 + \mathbf{k}_2 - \mathbf{k}_3$ show a characteristic peak pattern for each motiff. Resolution is enhanced by applying specific polarization configurations of the optical fields to oriented peptides.

I. Introduction

A central paradigm in structural biology is that the structure and function of biomolecules are intimately related.[1] Predicting structures of proteins requires understanding the forces and mechanisms which cause them to fold from a disordered, random coiled state into a unique native structure. Exploring the folding mechanism in detail requires tools which can probe the structures in real time with adequate temporal and spatial resolution for the dynamical event of interest. An ideal tool should also be sensitive to the important forces and environmental perturbations, for example, hydrogen bonding fluctuations during the process.

Techniques such as X-ray crystallography[2,3] and nuclear magnetic resonance (NMR)[4−6] provide the most useful atomic resolution information; however, NMR can only provide direct real time information on a millisecond time scale;[6] nanosecond processes may be sometimes probed indirectly through the frequency dependence of relaxation rates.[7] Time-resolved X-ray diffraction is currently carried out with a picosecond resolution.[7] Rapid progress in ultrafast X-ray technology could push this to the attosecond regime.[7]

Vibrational infrared and Raman spectroscopy is widely used for probing nuclear motions in proteins.[8−11] Vibrational transitions are ideal for distinguishing between various secondary structural motiffs and inspecting the effects of the changing environment through hydrogen bonding and dielectric effects. The 20 cm^{-1} variation of the 1600−1700 cm^{-1} amide I frequency (originating from the stretching motion of the C═O peptide bond coupled to in-phase N−H bending and C−H stretching) with secondary structure and conformation is widely used for studying the structure and dynamics of polypeptide and protein.[12−19] UV resonance Raman[20] and vibrational circular dichroism[21,22] are complimentary methods for studying the same amide transitions. The absorption line shapes provide information about dynamics.

Over the past decade, ultrafast IR spectroscopy has developed into a powerful structure and dynamics determination technique.[23−25] The signals displayed as two-dimensional correlation plots of various time delays contain more detailed and specific information compared with ordinary one-dimensional spectra: diagonal peaks in two-dimensional spectra show different transitions, cross-peaks reveal the couplings among the chromophores, and line shapes reflect the interactions with the surroundings.[16,26−36] Currently available IR pulses can provide 50-fs snapshots of dynamical events. This is adequate for exploring ultrafast peptide and protein dynamic events such as energy relaxation and the early stages of protein folding. This time scale is further accessible to large-scale molecular dynamics (MD) simulations allowing microscopic modeling of these signals.[37−42]

Femtosecond IR pump−probe and dynamic hole burning experiments were recently used to investigate the vibrational relaxation and anharmonicity of the amide I vibrations in *N*-methylacetamide and three small globular proteins:[33] apamin, scyllatoxin, and bovine pancreatic trypsin inhibitor. It was shown that the vibrations are anharmonic with 16 cm^{-1} anharmonicity, and delocalized exciton states extend over 2 to 3 units (∼0.8 nm). Energy migration among various amide I states is slow compared with the 1.2-ps vibrational relaxation time scale. Recent theoretical[43] and experimental[27] work showed that ^{13}C and ^{18}O isotope substitutions at certain positions in polypeptide chains can isolate new spectral lines clearly distinguishable from the main exciton group.

In this article, we present a simulation study of the two-dimensional IR amide I band spectrum and correlate it with the structure of four ideal peptide secondary motifs: α helix, 3_{10} helix, antiparallel β sheet (ABS), and parallel β sheet (PBS)[12] (see Figure 1). Characteristic features of each structure are most clearly seen for periodic infinite systems. Such spectra can be calculated using band theory in $\mathbf{k}$ space, as is commonly done in molecular crystals. In real peptides, finite segments show local inhomogeneities and boundary effects which complicate the spectra by peak shifts, additional lines and line broadenings. We study large finite systems numerically and discuss boundary effects.

In section II, we present the modeling protocol for the structures and the vibrational exciton Hamiltonian.[30,44] The method for calculating the response functions is summarized in section III. Rotationally averaged orientational factors of the response functions are given in appendix A. Simulations were carried out for two techniques: $\mathbf{k}_I = -\mathbf{k}_1 + \mathbf{k}_2 + \mathbf{k}_3$ (photon echo) where fundamental transitions show as diagonal peaks, while cross-peaks reveal correlations of fundamental peaks, and $\mathbf{k}_{III} = +\mathbf{k}_1 + \mathbf{k}_2 - \mathbf{k}_3$ which directly probes the two-exciton manifold. Both isotropic and oriented ensembles of the ideal structures are studied using various polarization configurations

10.1021/jp047711u CCC: $27.50
Published on Web 10/22/2004

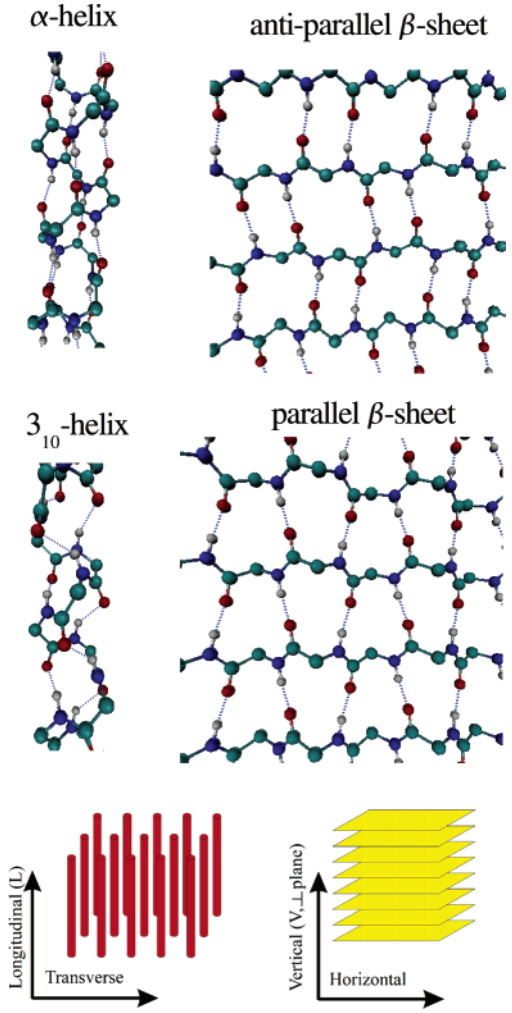

Figure 1. Top: The four structural motiffs of peptides used in this study. α and 3_{10} helices are one-dimensional structures, while ABS and PBS are two-dimensional. Green, C atoms; red, O atoms; blue, N atoms; and grey, H atoms. Bottom: polarization directions for oriented samples. Helices: longitudinal (l) along the axis and transverse (t). Sheets: horizontal (h, in plane) and vertical (v, normal).

of the optical fields. The simulations are presented in section IV and are discussed in section V.

II. Vibrational Exciton Hamiltonian

The third-order response to resonant IR optical fields was calculated using the vibrational exciton Hamiltonian:[30,45,46]

$$\hat{H}_S = \sum_m \epsilon_m \hat{B}_m^\dagger \hat{B}_m + \sum_{mn}^{m\neq n} J_{mn} \hat{B}_m^\dagger \hat{B}_n - \sum_{mn} \frac{\Delta_{mn}}{2} \hat{B}_m^\dagger \hat{B}_n^\dagger \hat{B}_m \hat{B}_n \quad (1)$$

Here, $\hat{B}_m^\dagger$ ($\hat{B}_m$) is the creation (annihilation) operator for mode m with frequency ϵ_m. These operators satisfy the Bose commutation relations $[\hat{B}_m, \hat{B}_n^\dagger] = \delta_{mn}$. J_{mn} is the harmonic intermode coupling, and Δ_{mn} is an anharmonicity. Diagonal anharmonicities Δ_{mm} represent the shift of the overtone energy from $2\epsilon_m$ for each vibrational mode. Off-diagonal intermode anharmonicities, Δ_{mn}, with $m \neq n$ lead to shifts of the combination band ($\hat{B}_m^\dagger \hat{B}_n^\dagger|0\rangle$) energies from $\epsilon_m + \epsilon_n$.

Hamiltonian for Helices. The ideal helical structure of a 22-residue strand ACE-$(ALA)_{20}$-NME was constructed using the graphic user interface Maestro in the Macromodel package.[47] The Ramanchandran angles taken from ref 12 are listed in Table 1. Geometry optimization was then performed using the PRCG[48]

TABLE 1: Ramanchandran Angles of the Ideal Structures of Four Motiffs

	α helix	3_{10} helix	PBS	ABS
ϕ	−57.0	−49.0	−119.0	−139.0
ψ	−47.0	−26.0	113	135

algorithm where the Ramanchandran angles were constrained at their ideal values. The Amber* force field[47] was used, and the convergence threshold was set to be 0.001 kJ/mol. Atomic coordinates of ideal structures used to construct the Hamiltonian were extracted from the central 18-residue part.

We assume the fundamental amide I frequency without H bonding to be 1710 cm^{-1}. To describe the H bonding effects on the amide I mode we distinguish between "direct" and "indirect" H bonds. The amide I transition is primarily C═O stretch, thus, a hydrogen bond involving the carbonyl O atom is defined as a "direct" H bond: **C═O**···H—N. This bond is expected to have a larger effect on the amide I frequency than a hydrogen bond connected to the N—H group in the same peptide unit, which will be denoted "indirect": O···H—N—**C═O**. Hydrogen bond was assumed to exist when the distance between oxygen and nitrogen is smaller than 2.6 Å and the O—N—H angle is smaller than 30°.[49] We assume that the direct and indirect hydrogen bonds induce a 20 and 15 cm^{-1} red shift of the mode frequency, respectively, and that the two shifts are additive.[13] Three (two) residues at each end of the α (3_{10}) helix have only one H bond to the other residues, while inner residues have two hydrogen bonds. Direct and indirect hydrogen bonding exist on different ends of both helices.

The couplings J_{mn} between peptide residues are determined by the transition charge densities (i.e., the derivatives of the charge density distribution with respect to various localized vibrations).[50] Amide I charge densities of distant residues do not overlap and the IR coupling is electrostatic.[51−53] Electron exchange cannot be ruled out for nearest neighbor (n-n) residues; J_{mn} must then be calculated at the ab initio level. We used Tasumi's ab initio map[54] for the couplings of nearest covalently bound modes. All other couplings were calculated using the electrostatic transition dipole coupling (TDC) model:[54]

$$J_{mn} = \frac{0.1}{\epsilon} \frac{(\boldsymbol{\mu}_m \cdot \boldsymbol{\mu}_n) - 3[\boldsymbol{\mu}_m \cdot \mathbf{e}_{mn}][\boldsymbol{\mu}_n \cdot \mathbf{e}_{mn}]}{r_{mn}^3} \quad (2)$$

where $\boldsymbol{\mu}_m$ is the transition dipole in (D $Å^{-1}$ $u^{-1/2}$) units, r_{mn} is the distance between dipoles in Å, $\mathbf{e}_{mn}$ is the unit vector connecting m and n, and $\epsilon = 1$ is the dielectric constant. The angle between the transition dipole and the C═O bond is 10°.[54]

The α helix repeat unit contains 18 residues (5 loops with 3.6 residues in each loop) and 3 residues for the 3_{10} helix (1 loop with 3 residues). However, in an ideal system each residue has identical couplings to its neighbors (except for the edge groups) because the coupling strength only depends on the relative orientations of the two dipoles. Small fluctuations of dihedral angles in the constructed helices induce variations in the calculated couplings. We, therefore, used the couplings of the 10th mode (at the center of the strand) with the other modes to represent couplings of all modes.

***β* Sheet Hamiltonian.** For each of the two β sheets, a 12-residue strand ACE-$(ALA)_{10}$-NME was first constructed and replicated 10 times to obtain 12 × 10 ABS and PBS. The unit cell of ABS contains four residues (*a*, *b*, *c*, and *d* in Figure 2). The central 8 × 8 residues of the structures were used to extract atomic coordinates of the ideal systems which were then used to compute the Hamiltonian.

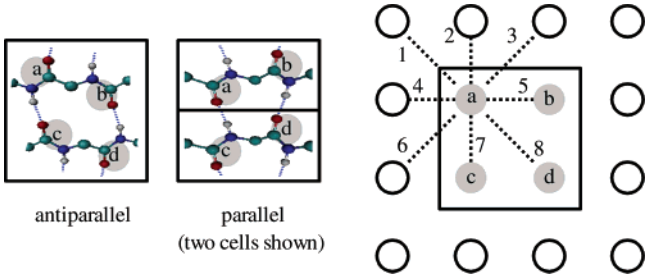

Figure 2. Left: unit cell for ABS with four residues. Middle: two unit cells for PBS (two residues per cell). The four sites denoted by *a*, *b*, *c*, and *d* are used to represent different residues in our simulations. Right: coupling scheme for site *a* of the ABS. The same coupling scheme is used for all sites in the unit cell and for the PBS.

TABLE 2: Coupling Strengths in cm^{-1} of Residue *n* with the Others in Two Helices[a]

	α helix	3_{10} helix		α helix	3_{10} helix
$J_{n,(n+1)}$	8.167	2.046	$J_{n,(n+5)}$	−1.666	−1.210
$J_{n,(n+2)}$	−3.155	−9.651	$J_{n,(n+6)}$	−1.642	
$J_{n,(n+3)}$	−12.657	−4.089	$J_{n,(n+7)}$	−1.140	
$J_{n,(n+4)}$	−4.139	−1.541			

[a] The couplings with an absolute value smaller than 1 cm^{-1} were neglected.

TABLE 3: Coupling Strengths J_{mn} in cm^{-1} of Residues *a*−*d* with the Neighbors Defined in Figure 2 for ABS

	a	*b*	*c*	*d*
1	−3.189	2.911	8.091	1.758
2	−14.049	−14.062	−14.063	−14.044
3	8.075	1.760	−3.187	2.911
4	2.672	2.672	2.672	2.672
5	2.672	2.672	2.672	2.672
6	2.910	−3.187	1.760	8.074
7	−14.063	−14.044	−14.070	−14.059
8	1.758	8.090	2.913	−3.195

The residues of the two outermost strands of the sheet have only one hydrogen bond with other strands. Inner residues have two H bonds in the sheets. ABS and PBS have alternating direct and indirect hydrogen bonding structure in outermost strands. H-bond shifts and the fundamental frequencies were assigned in the same way as for the helix. We included the n-n and next n-n couplings in the square lattice as shown in Figure 2. J_{mn} were calculated using the same procedure as for the helices. The same procedure was repeated for PBS, which has two residues per unit cell (Figure 2).

The coupling constants obtained from TDC and ab initio calculation for n-n sites are given in Tables 2−4. The structures created by geometry optimization have small fluctuations of the dihedral angles. Therefore, identical couplings (such as c3 and d8 for ABS in Figure 2) were averaged before the Hamiltonian was created.

Interaction with the Optical Field. The dipole coupling with the optical field $\mathbf{E}(t)$ is $\hat{H}_{SF} = -\mathbf{E}(t)\cdot\hat{\mathbf{P}}$, where $\hat{\mathbf{P}}$ is the polarization operator:

$$\hat{\mathbf{P}} = \sum_m \boldsymbol{\mu}_m(\hat{B}_m^\dagger + \hat{B}_m) \tag{3}$$

and $\boldsymbol{\mu}_m$ are the transition dipole moments. A fixed rotation of transition dipoles around the helical axis by 100° for α helix and 120° for 3_{10} helix for each residue were assumed. The angle between helical symmetry axis and the transition dipole is 24.24° for α helix and 33.93° for 3_{10} helix. Averaged directions of transition dipole vectors were assigned to all identical residues

TABLE 4: Coupling Strengths J_{mn} in cm^{-1} of Residues *a*−*d* with the Neighbors Shown in Figure 2 for PBS

	a	*b*	*c*	*d*
1	2.545	2.238	2.543	2.256
2	−14.068	−14.021	−14.072	−14.038
3	2.541	2.229	2.539	2.194
4	1.800	1.800	1.800	1.800
5	1.800	1.800	1.800	1.800
6	2.202	2.539	2.233	2.534
7	−14.072	−14.038	−14.048	−14.025
8	2.256	2.544	2.270	2.550

in both sheets. All transition dipoles were assumed to have the same magnitude $\mu_0 = 1$. Diagonal anharmonicity was assumed to be identical for all residues $\Delta_{mm} = \Delta = 16$ cm^{-1}, and off-diagonal anharmonicities Δ_{mn} were neglected.

Because Δ, $J_{m,n} \ll \epsilon_m$, the eigenstates of this Hamiltonian form two manifolds: a one-exciton manifold where one residue is excited to the first excited state and a two-exciton manifold where either two residues are excited to the lowest excited state (combination state) or when one residue is doubly excited (overtone). The Hamiltonian matrix was created in the basis set which includes the ground state $|0\rangle$, one-exciton excited states $\hat{B}_m^\dagger|0\rangle$, and two-exciton excited states $\hat{B}_m^\dagger\hat{B}_n^\dagger|0\rangle$. Calculations were carried out for infinite systems and for large finite segments. For infinite systems, we created a one-exciton Hamiltonian of 18 residue helices and 4 × 4 residue sheets. Translational invariance was then introduced by using cyclic boundary conditions for the couplings and identical diagonal energies (1675 cm^{-1}) for all residues. Large segments were simulated by computing the eigenstates for helices with 90 residues (5 unit cells of α helix and 30 unit cells of 3_{10} helix) and for sheets containing 10 × 10 residues (25 unit cells of ABS and 50 unit cells of PBS). This results in 4186 states for the helices and 5151 states for the sheets (one-exciton, two-exciton excited states + ground). The Hamiltonian matrix was diagonalized numerically yielding one-exciton eigenstates, denoted i, j with frequencies Ω_i, Ω_j and two-exciton eigenstates $\bar{\imath}, \bar{\jmath}$ with frequencies $\Omega_{\bar{\imath}}$ and $\Omega_{\bar{\jmath}}$. The transition dipole matrix was also created in the same basis and then transformed to the exciton basis using eigenvectors of the Hamiltonian matrix leading to new transition dipole vectors between the ground state and the one-exciton manifold $\mathbf{d}_i$ and between the one-exciton and the two-exciton manifold $\mathbf{d}_{i,\bar{\jmath}}$.

III. Third-Order Infrared Response

We shall briefly summarize the sum over states expressions used for calculating the coherent response.[55,56] The linear polarization induced by an optical electric field $E_\alpha(t)$ is given by the linear response function $S_{\nu,\alpha}^{(1)}(t_1)$:

$$P_\nu^{(1)}(t) = \sum_\alpha \int_0^\infty \mathrm{d}t_1\, S_{\nu,\alpha}^{(1)}(t_1)\, E_\alpha(t - t_1) \tag{4}$$

where Greek indices indicate Cartesian components, $\alpha,\nu = \{x, y, z\}$ with unit vectors $\mathbf{e}_\nu$. The response function is given by a sum over optical transitions from the ground state:

$$S_{\nu,\alpha}^{(1)}(t_1) = \mathrm{i}\theta(t_1)[\sum_j (\mathbf{e}_\nu\cdot\mathbf{d}_j)(\mathbf{e}_\alpha\cdot\mathbf{d}_j)\exp(-\mathrm{i}\Omega_j t_1 - \Gamma t_1) - \text{c.c.}] \tag{5}$$

where $\theta(t_1) = 0$ when $t_1 < 0$ and $\theta(t_1) = 1$ when $t_1 > 0$, c.c. denotes a complex conjugate, and Γ is a dephasing rate. The

linear susceptibility is given by the Fourier transform of the response function:

$$\chi^{(1)}_{\nu,\alpha}(\omega) = \int_0^\infty \mathrm{d}t_1\, S^{(1)}_{\nu,\alpha}(t_1)\exp(\mathrm{i}\omega t_1) = \sum_j \frac{2\Omega_j(\mathbf{e}_\nu\cdot\mathbf{d}_j)(\mathbf{e}_\alpha\cdot\mathbf{d}_j)}{\Omega_j^2 - (\omega + \mathrm{i}\Gamma)^2} \quad (6)$$

The linear absorption spectrum of an isotropic system is obtained by averaging the susceptibility over different rotations of the system (S) and over different polarizations of the signal:

$$\sigma_a(\omega) = \frac{4\pi\omega}{c\bar{n}} R_S\{\mathrm{Im}\,\chi^{(1)}_{\nu,\alpha}(\omega)\} \propto \sum_j \frac{\omega|\mathbf{d}_j|^2}{(\omega - \Omega_j)^2 + \Gamma^2} \quad (7)$$

where $R_S\{...\}$ denotes the averaging procedure (see appendix A), c is the speed of light, and $\bar{n}$ is the refraction index. The broadening parameter, Γ, was set to 1 cm^{-1} in all calculations.

The third-order polarization is given by

$$P^{(3)}_\nu(t) = \sum_{\gamma\beta\alpha}\int_0^\infty \mathrm{d}t_3 \int_0^\infty \mathrm{d}t_2 \int_0^\infty \mathrm{d}t_1\, S^{(3)}_{\nu,\gamma\beta\alpha}(t_3, t_2, t_1)\, E_\gamma(t - t_3)\, E_\beta(t - t_3 - t_2)\, E_\alpha(t - t_3 - t_2 - t_1) \quad (8)$$

The response function $S^{(3)}_{\nu,\gamma\beta\alpha}(t_3, t_2, t_1)$ is a fourth rank tensor and t_j are the intervals between successive interaction times with the various fields (see Figure 3). The response function is obtained by multiple summations over the eigenstates [eqs (5.19), (5.20), and (5.26) in ref 56].

There are four possible third-order signals, generated in the directions: $\mathbf{k}_I = -\mathbf{k}_1 + \mathbf{k}_2 + \mathbf{k}_3$, $\mathbf{k}_{II} = \mathbf{k}_1 - \mathbf{k}_2 + \mathbf{k}_3$, $\mathbf{k}_{III} = \mathbf{k}_1 + \mathbf{k}_2 - \mathbf{k}_3$, and $\mathbf{k}_{IV} = \mathbf{k}_1 + \mathbf{k}_2 + \mathbf{k}_3$. The rotating wave approximation may be used to select the dominant resonant terms for each technique.[55] $\mathbf{k}_I$, $\mathbf{k}_{II}$, and $\mathbf{k}_{III}$ involve one-exciton and two-exciton states, while $\mathbf{k}_{IV}$ also depends on three-exciton states. $\mathbf{k}_{II}$ carries information similar to that of $\mathbf{k}_I$ for our model, and the $\mathbf{k}_{IV}$ signal is typically weaker than the others because it requires higher anharmonicities. We, therefore, only simulated the resonant one-color signals $\mathbf{k}_I$ and $\mathbf{k}_{III}$.

Feynman diagrams depict the resonant terms for the density matrix (Figure 3) contributing to the response function. The two vertical lines in the diagram represent the evolution of the density matrix (time goes from the bottom to the top), while arrows represent interactions with the optical field. For detailed rules, see ref 55. Three diagrams contribute to $\mathbf{k}_I$. Two (a and b) involve only one-exciton transitions. The first diagram in Figure 3a shows absorption of the photon on the *bra* (negative wave vector, $-\mathbf{k}_1$, points to the left, while positive, $+\mathbf{k}_2$, points to the right) during the first interaction which puts the system into $|0\rangle\langle j|$ coherence. The second interaction (on the *ket*) represents the absorption of the second photon. It puts the system either in $|j'\rangle\langle j|$ coherence or into $|j\rangle\langle j|$ population. The third interaction shows photon emission on the *bra*. After this interaction, the system is in the coherence $|j'\rangle\langle 0|$. The measurement is represented by the last interaction, which leaves the system in a population. The contribution of the diagram to the optical response function is $(-1)^p\hat{\xi}(j'0, j0, 0j', 0j)\exp[-\mathrm{i}(\omega_{0,j}t_1 + \omega_{j',j}t_2 + \omega_{j',0}t_3) - \Gamma(t_1 + t_2 + t_3)]$ if $j' \neq j$ and $(-1)^p\hat{\xi}(j'0, j0, 0j', 0j)\exp[-\mathrm{i}(\omega_{0,j}t_1 + \omega_{j,0}t_3) - \Gamma(t_1 + t_3)]$ if $j' = j$, where $\omega_{j',j} = \Omega_{j'} - \Omega_j$, Γ is the line width parameter for the transition, and $\hat{\xi}(i, j, k, l) = (\mathbf{d}_l\cdot\mathbf{e}_\nu)(\mathbf{d}_k\cdot\mathbf{e}_\gamma)(\mathbf{d}_j\cdot\mathbf{e}_\beta)(\mathbf{d}_i\cdot\mathbf{e}_\alpha)$ is the orientation factor. p is the number of interactions on the right side of the density matrix. Other diagrams can be interpreted in a similar way. The third diagram (c) also includes two-exciton states. Diagrams d and e contribute to $\mathbf{k}_{III}$. Both involve the two exciton states, and during t_2 the system is in the coherence $|\bar{j}\rangle\langle 0|$. This technique is, therefore, an excellent direct probe for two-exciton states.

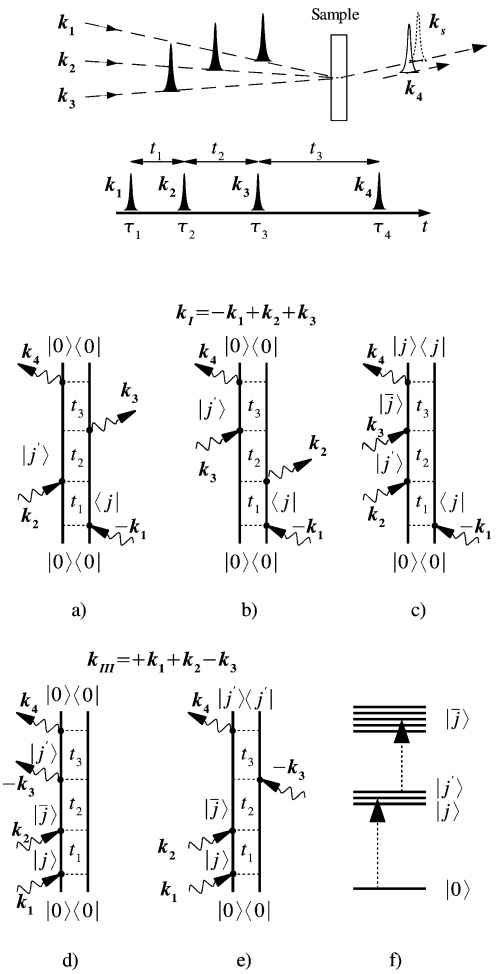

Figure 3. Pulse sequence in a third-order experiment. Three pulses with wavevectors $\mathbf{k}_1$, $\mathbf{k}_2$, and $\mathbf{k}_3$ (in chronological order) interact with the sample to create a coherent optical signal with wavevector $\mathbf{k}_s = \pm\mathbf{k}_1 \pm \mathbf{k}_2 \pm \mathbf{k}_3$. By varying the time delays, each technique can selectively probe various coherences in the system. (a−c) Feynman diagrams for $\mathbf{k}_I$, (d, e) Feynman diagrams for $\mathbf{k}_{III}$. (f) The energy level scheme.

We shall display the $\mathbf{k}_I$ signal by transforming the response function $S_{\nu,\gamma\beta\alpha}(t_3, t_2, t_1)$ to the frequency domain with respect to t_1 and t_3:

$$W^{(3)}_{I,\nu,\gamma\beta\alpha}(\omega_1, t_2, \omega_3) = \left|\int_0^\infty\int_0^\infty \mathrm{d}t_1\, \mathrm{d}t_3\, S^{(3)}_{I,\nu,\gamma\beta\alpha}(t_3, t_2, t_1)\exp(\mathrm{i}\omega_1 t_1 + \mathrm{i}\omega_3 t_3)\right| \quad (9)$$

Similarly, the $\mathbf{k}_{III}$ signal will be displayed by performing a Fourier transform with respect to t_2 and t_3:

$$W^{(3)}_{III,\nu,\gamma\beta\alpha}(t_1, \omega_2, \omega_3) = \left|\int_0^\infty\int_0^\infty \mathrm{d}t_2\, \mathrm{d}t_3\, S^{(3)}_{III,\nu,\gamma\beta\alpha}(t_3, t_2, t_1)\exp(\mathrm{i}\omega_2 t_2 + \mathrm{i}\omega_3 t_3)\right| \quad (10)$$

For oriented ensembles, a Z axis was defined for each system (Figure 1). The Z axis of the helices is longitudinal (L) along the helix axes, while for the sheet it is normal (vertical, V) to the plane of the sheet. The response tensors were rotationally averaged with respect to the optical field (see appendix A). To

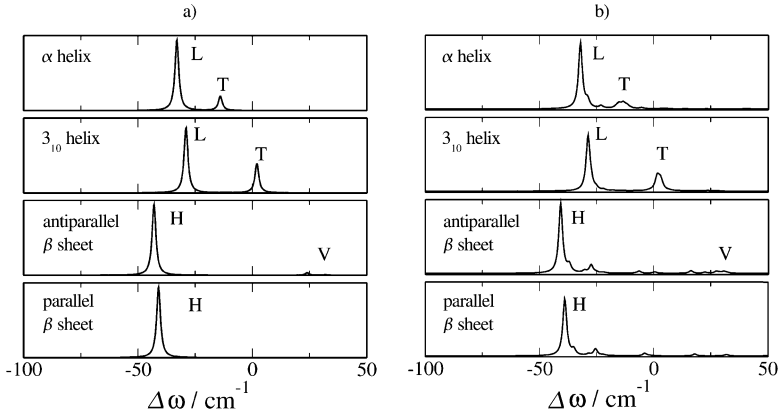

Figure 4. Simulated linear absorption spectra of the four ideal infinite (a) and large finite (b) motiffs. The frequency origin is 1675 cm^{-1} ($\Delta\omega = \omega - 1675$ cm^{-1}). L and T mark longitudinal and transverse transitions for the helices, while H and V mark horizontal and vertical transitions of the sheets.

TABLE 5: Transitions between the Ground and One-Exciton States in the Translationary Invariant Systems with Cyclic Boundary Conditions[a]

	Ω, cm^{-1}	$\boldsymbol{\mu}_x/\mu_0$	$\boldsymbol{\mu}_y/\mu_0$	$\boldsymbol{\mu}_z/\mu_0$
18 residue α	1642	0	0	3.9
	1661	1.22	−0.18	0
	1661	0.18	1.22	0
18 residue 3$_{10}$	1646	0	0	3.5
	1677	−1.41	0.89	0
	1677	−0.89	−1.41	0
4 × 4 residue aβ	1662	3×10^{-4}	3×10^{-4}	−0.04
	1699	0.73	0.05	-8×10^{-3}
	1707	-8×10^{-5}	-5×10^{-3}	0.38
	1632	0.23	−3.9	−0.05
4 × 4 residue pβ	1660	−0.04	−0.03	−0.06
	1634	2.5	−3	0.14

[a] "α" stands for α helix, "3$_{10}$" for 3$_{10}$ helix, "aβ" for ABS, and "pβ" for PBS. The *Z* direction was defined in Figure 1, while *X* and *Y* are arbitrary because we perform rotational averaging over these coordinates when calculating the optical response.

simulate isotropic samples, we performed full rotational averaging, while for oriented samples we carried out partial rotational averaging around the *Z* axis.

IV. Simulation Results

A. α and 3$_{10}$ Helices. Infinite system simulations presented in Table 5 show three optically allowed transitions between the ground and one-exciton manifold: one longitudinal and two degenerate (transverse). Each helix has two peaks in the linear absorption spectrum shown in the first two rows of Figure 4a.

All other simulations were carried out for large finite segments. Scatter plots of the distribution of one-exciton eigenstates shown in the first two rows of Figure 5 present the possible transitions from ground to one-exciton manifold. Two groups of states can be reached by either longitudinal L or transverse T. The former have stronger transition dipoles and lower frequencies. Thus, the distribution of states in Figure 5 results from boundary effects, while the L and T groups correspond to the longitudinal and transverse transitions of the infinite system (see Table 5 and Figure 4a).

The two-exciton states can also be sorted out according to their transition dipoles to the various groups of one-exciton states. To that end we define the quantity

$$(\bar{\mu}_{\bar{\imath}}^{(1,2)})_\kappa = \sqrt{\sum_{i\in g} |(\mathbf{d}_{i,\bar{\imath}})_\kappa|^2} \qquad (11)$$

which shows the relative strength of the total transition to the two-exciton state $\bar{\imath}$ from each group, g = L, T, of one-exciton states with polarization κ: for longitudinal L we use $(\mathbf{d}_{i,\bar{\imath}})_L = (\mathbf{d}_{i,\bar{\imath}})_z$ and for transverse $(\mathbf{d}_{i,\bar{\imath}})_T \equiv (\mathbf{d}_{i,\bar{\imath}})_{xy} = [(\mathbf{d}_{i,\bar{\imath}})_x^2 + (\mathbf{d}_{i,\bar{\imath}})_y^2]^{1/2}$. Scatter plots of the distribution of two-exciton states sorted by their energy and $\bar{\mu}^{(1,2)}$ are shown in Figure 6. L → L denotes the transitions between the one-exciton states within group L and two-exciton states with L polarization. α and 3$_{10}$ helices show similar distributions with three main groups in the two-exciton manifold selected by different polarizations: lowest energy group L → L, highest energy group T → T, and intermediate energy group L → T or T → L.

The calculated isotropic linear absorption [$\sigma_a(\omega)$] depicted in Figure 4b shows two peaks for the α helix. The stronger (1642.9 cm^{-1}) peak corresponds to the longitudinal transitions, and the higher energy peak at 1662 cm^{-1} contains few transverse transitions. The 3$_{10}$ helix spectrum is similar but with a larger splitting: 1646 cm^{-1} (longitudinal) and 1677 cm^{-1} (transverse).

The sum over states expressions for the third-order signal were truncated: if the absolute values of all transition dipoles connecting a state i with all the other states $j \neq i$ obeys the relation $\log(|\mathbf{d}_{ij}|/\mu_0) < 0$, the state was not included (μ_0 is the transition dipole of the isolated mode). This cutoff is shown by solid red lines in Figure 5.

We first consider the $\mathbf{k}_I$ signal $W_I^{(3)}(\omega_1, t_2 = 0, \omega_3)$ for two polarization configurations: zzzz and zzxx. The zzzz spectrum of an isotropic system of α helices (Figure 7) shows two diagonal one-exciton peaks. The cross-peaks which indicate correlations between these states are not well resolved because of overlap with the much stronger diagonal peaks. The cross-peaks are better resolved in the zzxx configuration (second column). The diagonal peak splitting is larger, and the cross-peaks are well resolved for 3$_{10}$ helices. Similar to those of the α helix, the cross-peaks are better resolved for zzxx indicating that the relevant transitions are not parallel (perpendicular transition dipoles give largest sensitivity to polarizations). If all transitions were parallel, the largest amplitude would be obtained with the zzzz configuration.

The $\mathbf{k}_{III}$ signal $W_{III}^{(3)}(t_1 = 0, \omega_2, \omega_3)$ which shows two-exciton states during the coherence time t_2 is depicted in Figure 8 for zzzz and zzxx. During t_3 the density matrix may have coherences either between the ground and the one-exciton states or between the one-exciton state and the two-exciton state. The peaks for the α helix are very close and overlap. Additional peaks are resolved for zzxx (highlighted by the circle). The 3$_{10}$ helix spectra show many well-resolved peaks. Three dominant two-

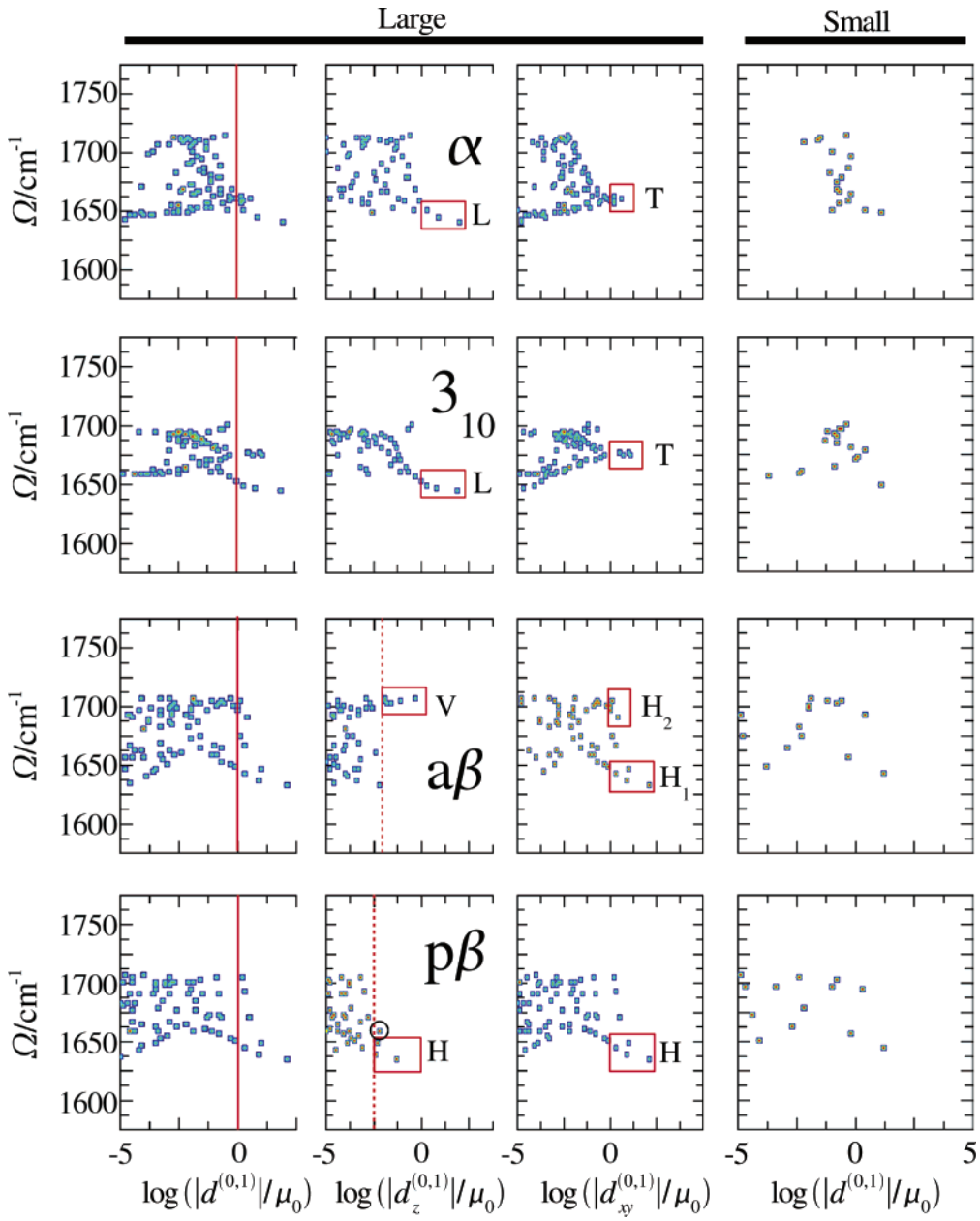

Figure 5. Statistical distribution of one-exciton transitions for the four structures: "α", α helix; "3_{10}", 3_{10} helix; "aβ", ABS; and "pβ", PBS. The vertical axis of each point represents the energy of a one-exciton state, and the horizontal axis shows the transition dipole connecting it with the ground state. The first column shows the total dipole amplitude, while the second and third columns represent *z* and *xy* components. Solid red lines represent the transition cutoff used for the selection of the states. Dotted red lines represent additional cutoffs used to select vertical transitions in the β sheets (see text). The results for 90 residue helical aggregates and 10 × 10 residue sheets are marked "Large". The results for smaller structures (18 residues for both helices and 16 residues for both sheets) are given on the right-most column, "Small", illustrating boundary effects for the total dipole.

exciton states can be identified; two are better resolved in the zzxx spectrum (highlighted by circles).

The resolution of the $\mathbf{k}_\mathrm{I}$ spectra is improved considerably for oriented samples (Figure 9). The longitudinal (transverse) peaks are selected by applying LLLL (TTTT) polarizations. Different cross-peaks (above or below the diagonal) are selected by using cross polarizations (LLTT or TTLL). These cross-peaks originate from the Feynman diagrams where the system is back in the ground state during the second interval t_2. The first two interactions create and annihilate the coherence of either longitudinal (LL polarization) or transverse (TT polarization) transitions. The latter two interactions have perpendicular polarization and create different coherences. Thus, only the cross-peaks in the spectrum are allowed provided the longitudinal and transverse transitions are perpendicular and have different transition energies. The diagonal peaks vanish in this case.

Polarization-sensitive simulations of $\mathbf{k}_\mathrm{III}$ in oriented samples show a distinct peak pattern (Figure 10) with two dominant groups of two-exciton states. The signals of the two helices are similar, but the peak splitting is larger for the 3_{10} helix.

B. ABS and PBS. The same simulation protocol was repeated for the sheets. Horizontal and vertical transitions were defined in Figure 1. The allowed transitions of infinite ABS and PBS are given in Table 5. In general, the number of transitions in ideal infinite aggregates is equal to the number of sites per unit cell (Davydov's components) which is 4 in the case of ABS. However, three transition dipoles (two horizontal at 1699 and

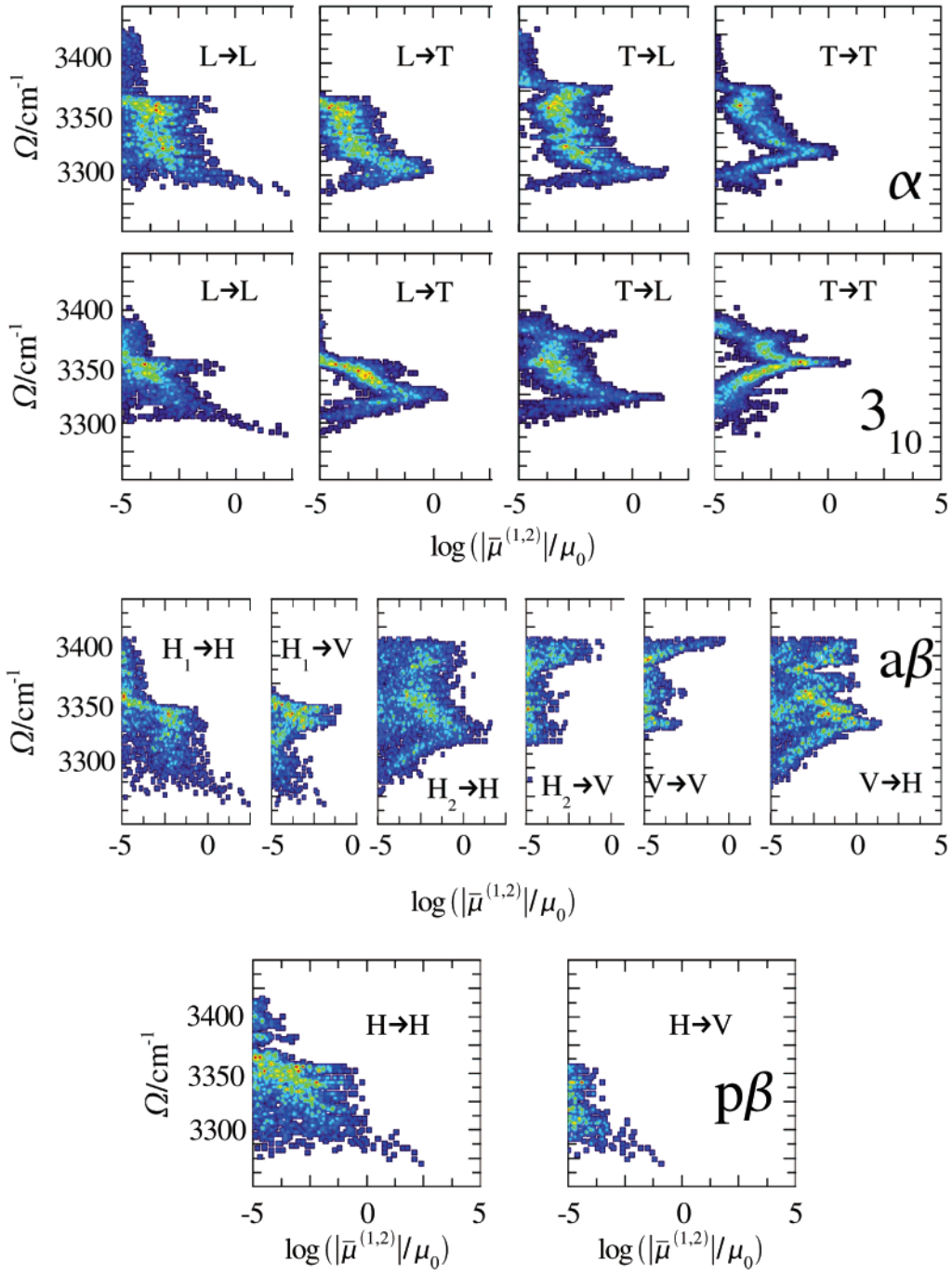

Figure 6. Statistical distribution of two-exciton transitions sorted by their origin from different groups of one-exciton states. Each point represents the energy of a one-exciton state (vertical axis) and the total transition strength from the group of one-exciton states (eq 11) on the horizontal axes. Blue/red color in the distribution represents low/high density of points when they are overlapping. Each row corresponds to different large structures indicated as in Figure 5. Different columns represents different polarization configurations and different one-exciton groups as explained in the main text.

1632 cm^{-1} and one vertical at 1707 cm^{-1}) are much stronger compared to the fourth at 1662 cm^{-1} as shown in Table 5. The PBS has two sites per unit cell and two possible transitions. As shown in Table 5 only one transition which is neither horizontal nor vertical is dominant (the angle of that transition dipole with the *XY* plane is 2°, however, the other transition has almost three times smaller vertical component), and, therefore, PBS can be considered as having only one excited state in the one-exciton manifold. The resulting linear absorption spectrum (third and fourth columns of Figure 4a) contains one strong transition for both sheets. Higher energy transitions can be observed for ABS.

The following simulations were carried out for finite large sheets. Similar to the finite helices, exciton states can be grouped for the large finite sheets. The ABS shows a strong horizontal transition in the scatter plots of the distribution of one-exciton eigenstates depicted in the third row of Figure 5 [for horizontal transition amplitude, we use $(\mathbf{d})_H \equiv (\mathbf{d})_{xy} = \sqrt{(\mathbf{d})_x^2+(\mathbf{d})_y^2}$ and for vertical $(\mathbf{d})_V = (\mathbf{d})_z$]. On the basis of the results for infinite systems, three groups of states can be defined for ABS: two horizontal (H_1 and H_2) and one vertical (V) as shown in Figure 5. PBS (fourth row in Figure 5) does not show different groups of states with different polarizations. The same states have high

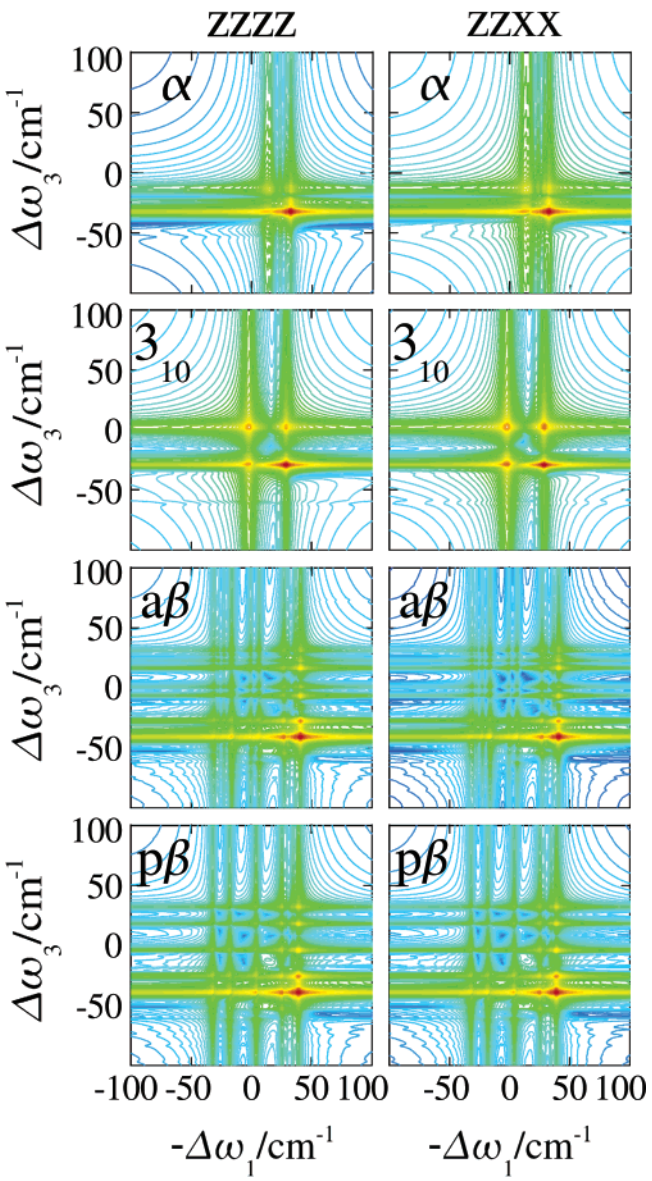

Figure 7. $\mathbf{k}_{\mathrm{I}}$ signal $W^{(3)}_{\mathrm{I},\nu,\gamma\beta\alpha}(\omega_1, t_2 = 0, \omega_3)$ (eq 9) of isotropic samples of the four structural motiffs for parallel (zzzz) and cross (zzxx) polarization configurations. Structures are labeled as in Figure 5. The frequency origin is 1675 cm^{-1} ($\Delta\omega_1 = -\omega_1 - 1675$ cm^{-1}, $\Delta\omega_3 = \omega_3 - 1675$ cm^{-1}).

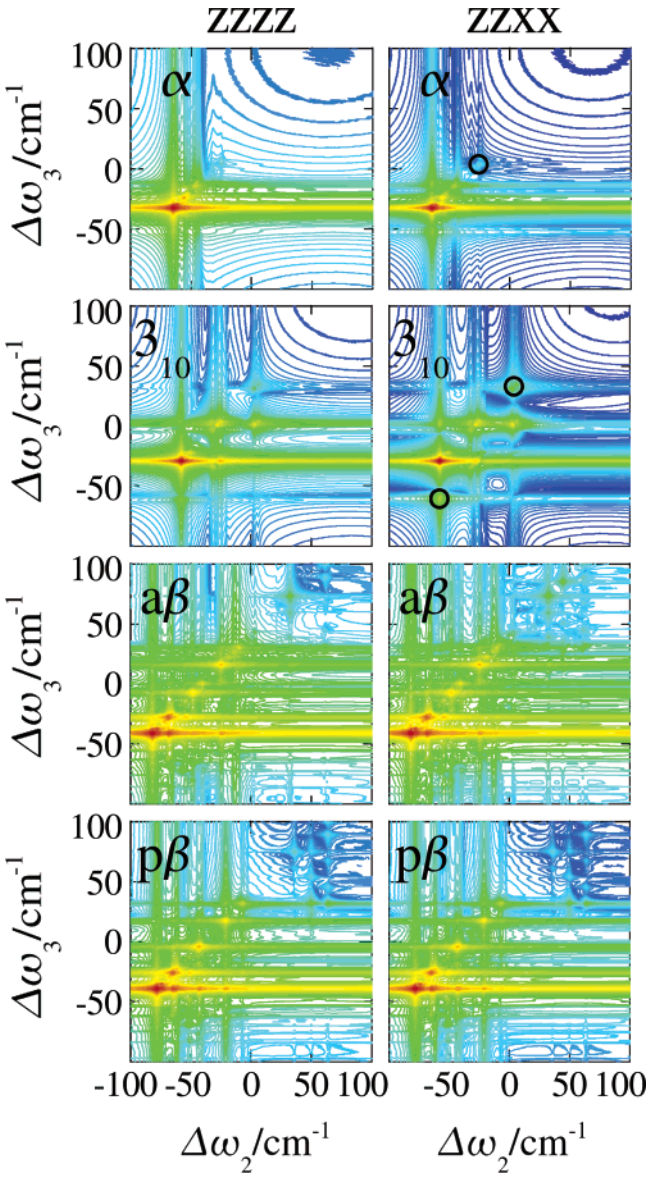

Figure 8. Same as Figure 7 but for the $\mathbf{k}_{\mathrm{III}}$ signal $W^{(3)}_{\mathrm{III},\nu,\gamma\beta\alpha}(t_1 = 0, \omega_2, \omega_3)$ (eq 10). The frequency origin is 2×1675 cm^{-1} for ω_2 and 1675 cm^{-1} for ω_3 ($\Delta\omega_2 = \omega_2 - 2 \times 1675$ cm^{-1}, $\Delta\omega_3 = \omega_3 - 1675$ cm^{-1}).

transition dipoles in H and V polarizations. We define only one group H which has a strong horizontal amplitude. The strongest strictly vertical transition circled in Figure 5 is very weak.

The two-exciton state distribution of ABS shown in the third row in Figure 6 is more complex compared to the helices. Different groups of two-exciton states can be clearly identified and selected by different polarizations: especially $H_1 \rightarrow H$ and $V \rightarrow V$ are well separated. Similar to the one-exciton manifold, the two-exciton distribution of PBS does not show selectivity to different polarizations.

The absorption spectrum of an isotropic ABS (Figure 4b) has one major peak at 1634 cm^{-1}. The overall distribution of peaks is broader than that of helices. The weaker vertical peak is around 1707 cm^{-1}. The spectrum of an isotropic ensemble of PBS shows a well-resolved H_1 transition at 1636 cm^{-1} and no vertical transition.

An additional cutoff was used to show the vertical transitions in the third-order simulations. The state is included provided $\log(|(\mathbf{d}_{ij})_z|/\mu_0) > c$ even if $\log(|\mathbf{d}_{ij}|/\mu_0) < 0$. The cutoffs $c = -2$ for ABS and $c = -2.5$ for PBS shown by the dotted red lines in Figure 5 were selected to best display the major transitions for different polarizations.

The peak pattern of $W^{(3)}_{\mathrm{I},z,zzz}(\omega_1, t_2 = 0, \omega_3)$ of both sheets (Figure 7) is similar but very different from that of the helices. The major diagonal peaks correspond to horizontal transitions which are almost at the same frequency for both sheets. The rich cross-peak pattern in the ABS contains also transitions to the vertical states. Similar results are for PBS. The zzxx polarization configuration does not improve the resolution because horizontal transitions are much stronger than vertical ones.

The $W^{(3)}_{\mathrm{III},z,zzz}(t_1 = 0, \omega_2, \omega_3)$ spectrum for the sheets (Figure 8) contains many one-exciton peaks. Two groups of peaks can be identified: (i) those originating from the major horizontal one-exciton transition and distributed at constant ω_3. These peaks reflect transitions between two-exciton state and the horizontal one-exciton state during the second interaction represented by the Feynman diagram in Figure 3d. (ii) The second group also originates from the same horizontal one-

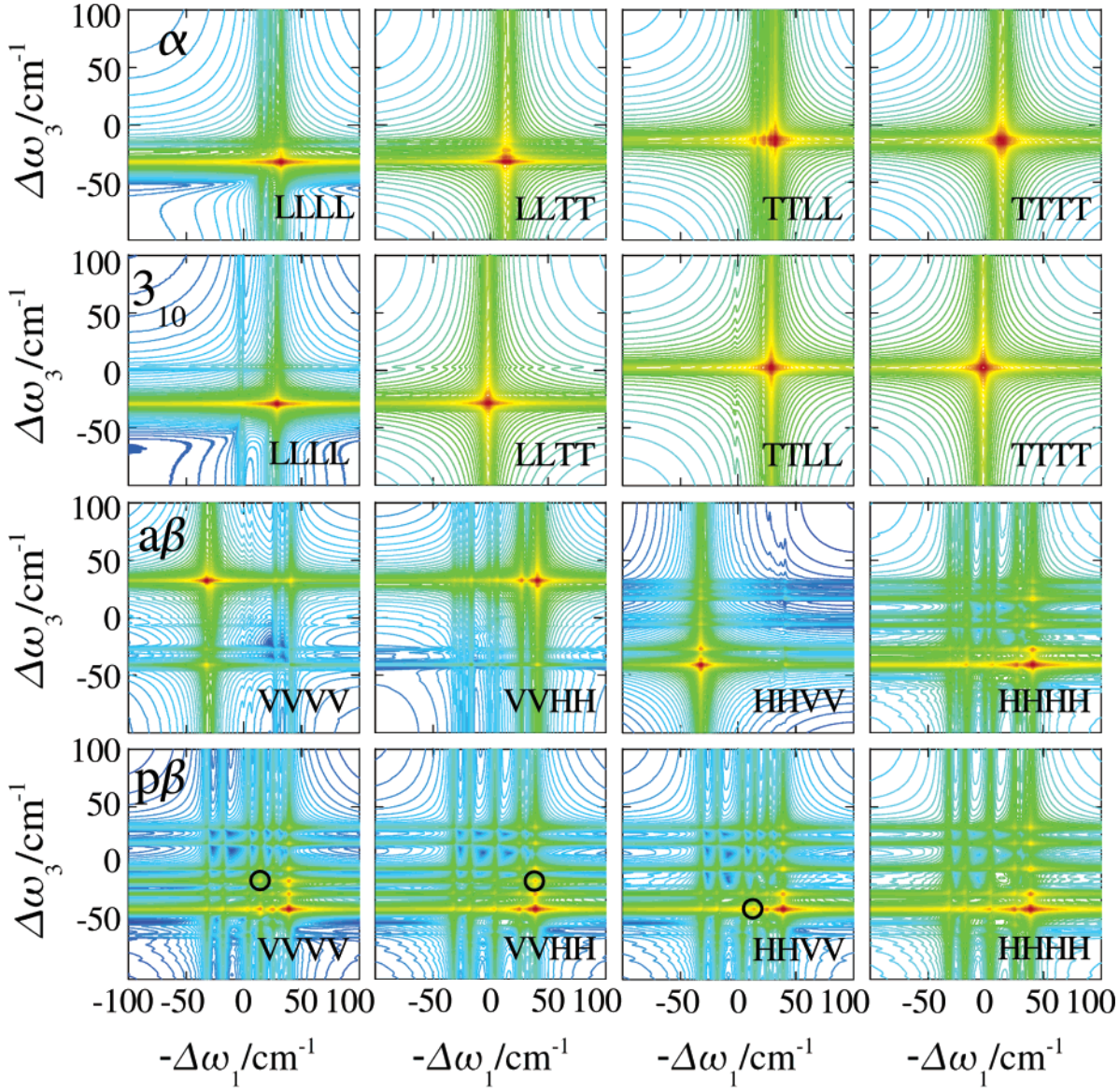

Figure 9. $\mathbf{k}_I$ signals. Same as Figure 7 but for oriented samples.

exciton transition and is distributed along the diagonal. These peaks reflect coherences between two-exciton states and the horizontal one-exciton state during the third time interval represented by diagram e in Figure 3. There are no qualitative differences between the PBS and the ABS.

Signals for oriented sheets are displayed in Figures 9 and 10. ABS clearly show well-resolved horizontal and vertical transitions and the corresponding cross-peaks using VVVV, VVHH, and HHVV optical polarizations in $W_I^{(3)}$ and $W_{III}^{(3)}$. The peak pattern is now different compared to the PBS where the polarizations do not make much difference. However, additional vertical peaks appear in the VVVV configuration with corresponding cross-peaks in HHVV and VVHH (circled in Figure 9) for the PBS. The HHHH configuration shows a pattern very similar to the isotropic system for both sheets. The ABS shows strong peaks related to vertical/horizontal transitions in $W_{III}^{(3)}$. One two-exciton state dominates the VVVV process, and the other two-exciton state is involved in the HHHH process. The HHVV and VVHH spectra demonstrate that two groups of two-exciton states are primarily involved in the response. PBS show poor sensitivity to different polarizations, however, one additional, while poorly resolved, peak appears in VVVV.

V. Discussion

We have calculated the nonlinear response of four ideal secondary structures of polypeptides. A different peak pattern is revealed in correlation plots of the signals which can be used for structure determination. The systems have a characteristic anisotropy which could be used to extract specific features in polarization-sensitive experiments. Different secondary structures show distinct correlation plots of nonlinear spectroscopic techniques. The linear absorption shows transitions from the ground to the one-exciton manifold. These spectra do not contain many details. Easily distinguishable transitions in the simulations may be difficult to resolve experimentally because of larger broadening.

Two-dimensional correlation plots reveal many more details. Diagonal peaks provide information about the transitions between the ground states and the one-exciton manifold. Information about couplings is contained in the cross-peaks, which show correlations between different peaks. Cross-peaks in helices indicate very strong correlations between longitudinal and transverse transitions, while for the ABS they show correlations between horizontal and vertical peaks. The other weaker cross-peaks in the sheets correspond to the boundary.

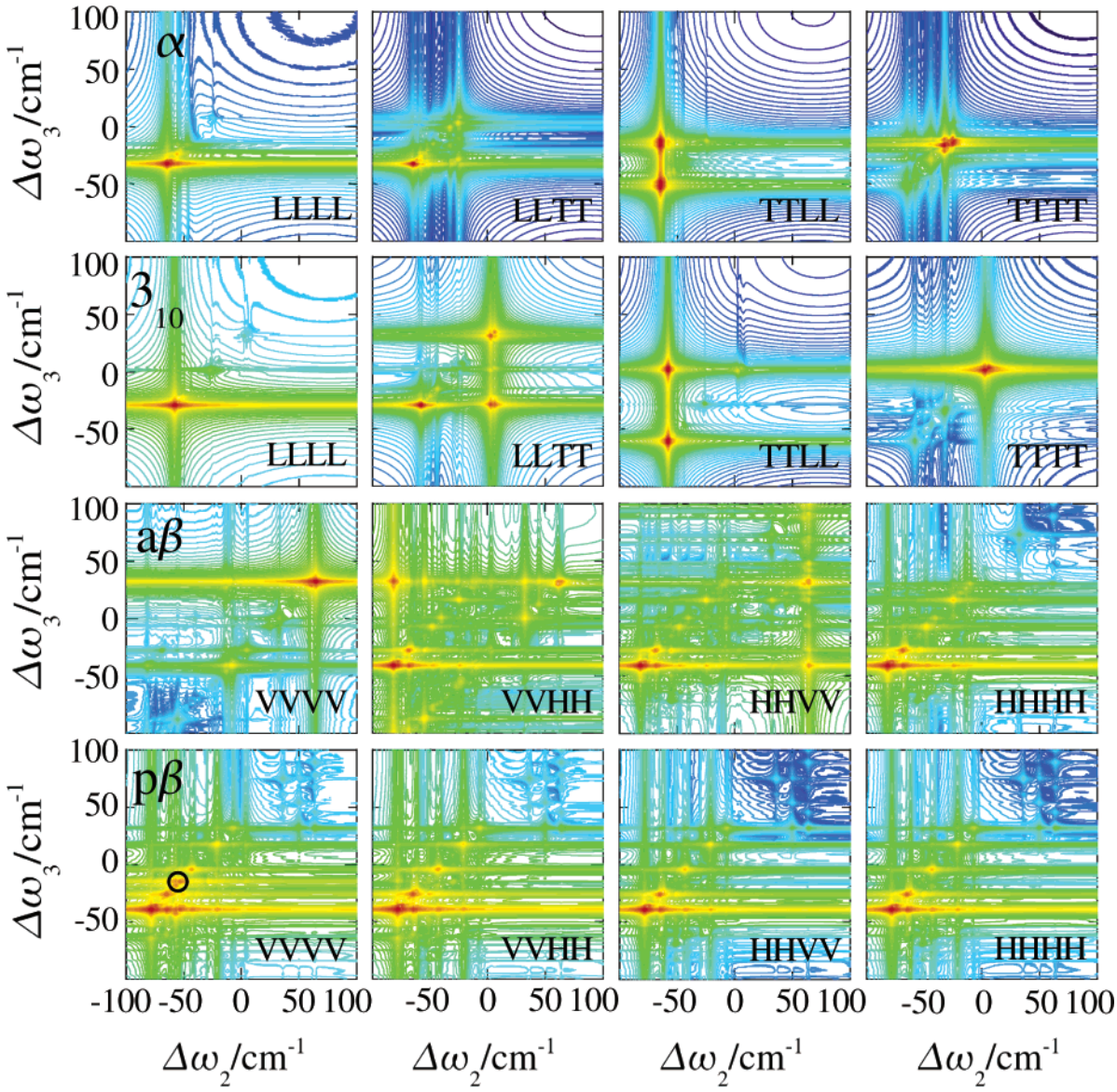

Figure 10. $\mathbf{k}_{III}$ signals. Same as Figure 8 but for oriented samples.

The resolution is considerably improved for oriented ensembles where different cross-peaks may be selected by controlling the polarizations. High resolution is achieved by turning off diagonal peaks in oriented α and 3_{10} helices. Diagonal peaks require polarizations where all four interactions with the same transition dipole have a finite scalar product **e**·**d**, where **e** is the polarization vector of the optical field and **d** is the transition dipole vector. This condition is not satisfied for cross-polarized spectra in oriented helices. This configuration is, however, favorable for cross-peaks between longitudinal and transverse transitions. This argument also applies to ABS where the transition dipoles of eigenstates create a distinct peak pattern because the vertical peak is well separated from the horizontal. PBS do not show these signatures. The reason is that the transition dipoles between the ground and one-exciton manifold in the PBS are neither horizontal nor vertical and, thus, the response function is not as sensitive to H or V polarizations as for another structures.

Additional high-resolution information is obtained from the $\mathbf{k}_{III}$ technique where the coherence between the two-exciton state and the ground state is generated during the second time interval t_2 and the two-exciton spectrum is observed along ω_2. While there are hundreds of two-exciton states, only a small fraction show up in the simulations.

One possible application of two-dimensional IR is for probing the structure of oriented samples of amyloid fibrils. These are ill characterized filamentous structures formed by a variety of peptides and proteins with widely distributed lengths and amino acid sequences.[57−61] Interest in the molecular structure of amyloid fibrils stems from their role in Alzheimer's disease and from the observation that this is a stable state of a very large class of polypeptides.[59−61] Real proteins which differ by the distribution of side groups and hydrogen bonding patterns are not expected to have the ideal structures simulated here. Fluctuation of the environment also creates energy and coupling shifts. Moreover, real structures often have short segments with turns while long-range fluctuations (for instance: bent helix or curled strands) are also found. We shall discuss these points below.

Our simulated peak positions correlate well with experiment. The average position of amide I peaks of α helix is 1647 cm^{-1}.[20] Our calculated longitudinal peak of α helix is very close to the experimental value. The transverse transitions have a lower amplitude and should cause a broader high frequency shoulder

for the amide I line if line broadening was included. ABS and PBS have a broad range of amide I frequencies in different proteins ranging from 1620 to 1640 cm^{-1}.[20,62−65] Our simulations are in that range. The broad distribution of frequencies may come from dielectric interactions of the mode with other parts of the system (peptide side groups, solvation effect). Recent two-dimensional IR spectroscopy predicts different types of peak patterns for the α helix and β sheet:[66] a "Z"-shaped pattern whose magnitude increases with the content of ABS fragments was observed. Empirical results obtained by the comparison of different proteins only give a qualitative description of different protein structures,[66] and the origin of different features for different structures remains an open issue. On the basis of our simulations, we believe that the "Z" shape is a result of line broadening showing different types of correlations between fluctuations of different amide transitions. Microscopic simulation of line broadening is one of our future goals. Weak frequency fluctuations may be responsible for the reduction of the exciton delocalization length which is important in one-dimensional systems.[67] However, the fine structure of the exciton states may not be resolved when the line width is larger than state spacing within the exciton bands. In this case the signal is no longer dependent on the size. As the size of the system is increased the eigenstate spacings become smaller while the line width remains essentially invariant.

Finite size effects are expected for small peptides. In general for one-dimensional helices we can assume M residues at the edge independent of the size N. The number of "interior" residues is $N - M$. For two-dimensional structures there are $2NM$ residues at two edges (the other two edges do have a complete hydrogen bonding structure in the β sheets), whereas the total number of residues is $N \times N$. For two-exciton states, the largest contribution comes from combinations, which scales less favorably: the number of "interior" combinations not involving edge groups is $(N - M)(N - M - 1)/2$ in one dimension, while it is $(N^2 - 2NM)(N^2 - 2NM - 1)/2$ in two dimensions. The crossing point when the number of interior residues is equal to the number of boundary residues with respect to one-exciton and two-exciton states indicates the size when edge effects may be neglected. For helices we have $M = 6$ (two or three residues at the end with different transition energies and the interaction range is also 3). Edge effects are then negligible for $N \gg 42$. For β sheets $M = 2$ (one strand of residues at the two edges with different transition energies and the interaction range is also 1). Then edge effects are negligible for $N \gg 8$. In Figure 5 (right column) we show the distribution of energy and transition dipoles to the ground state for one-exciton states in smaller systems: 18 residues for both helices and 4×4 residues for both sheets. The pattern is not as ordered as for the larger systems. Longitudinal transitions for the helices and horizontal transitions for the sheets may be identified, but other transition dipoles have no well-defined polarization even for helices.

In our simulations of helices with 90 residues, edge effects are negligible. For the β sheets, however, finite size effects are very strong and many weak peaks in the spectra are related to residues at the edges. Generally these can be determined in polarization-sensitive measurements because we expect that the peaks which come from inhomogeneities will not have well-defined polarization direction in oriented samples, while "interior" peaks have well-defined symmetry: L/T, H/V. The 10×10 sheets contain many cross-peaks which are present in all plots with different polarization configurations.

A more elaborate simulation protocol will be necessary to accurately model the spectrum of realistic globular proteins: the frequencies and couplings have to be assigned on the basis of the electrostatic field experienced by the chromophores; polarizable force fields can be used to assign partial charges to various parts of the peptide so that the optical response can be reproduced more accurately. Hydrogen bonding effects on the amide fundamental frequency need to be considered explicitly. A realistic line width can be calculated from MD simulations. These studies are in our future plans.

Acknowledgment. The support of the National Institutes of Health Grant 1 RO1 GM59230-03 is gratefully acknowledged. This material is based upon work supported by the National Science Foundation Grant CHE-0132571. We wish to thank Professor Charles Glabe for most useful discussions.

Appendix A: Rotational Averaging of Tensor Components

To simulate experiments in solution, rotational averaging of the orientational factors in the response functions must be performed. A complete three-dimensional rotational averaging of the linear response function results in averaging a quantity $\langle(\mathbf{a}\cdot\boldsymbol{\alpha})(\mathbf{b}\cdot\boldsymbol{\alpha})\rangle$ where vectors **a** and **b** are electric field unit vectors in the lab frame and $\boldsymbol{\alpha}$ is a transition dipole unit vector in the molecular frame. Orientational averaging over different rotations of the system leads to $\langle(\mathbf{a}\cdot\boldsymbol{\alpha})(\mathbf{b}\cdot\boldsymbol{\alpha})\rangle = \mathbf{a}\cdot\mathbf{b}$. Averaging over different polarizations of the signal (**a**) results in a constant factor, and the averaged linear absorption is polarization independent.

The third-order response function polarization dependent factor is $\langle(\mathbf{a}\cdot\boldsymbol{\alpha})(\mathbf{b}\cdot\boldsymbol{\beta})(\mathbf{c}\cdot\boldsymbol{\gamma})(\mathbf{d}\cdot\boldsymbol{\eta})\rangle$ (here vectors **a**, **b**, **c**, and **d** are electric field unit vectors in the lab frame and $\boldsymbol{\alpha}$, $\boldsymbol{\beta}$, $\boldsymbol{\gamma}$, and $\boldsymbol{\eta}$ are transition dipole unit vectors in the molecular frame). For complete three-dimensional averaging over different system rotations we use the expressions given in ref 68. To simulate oriented systems along the Z axis of the lab frame, we performed partial rotational averaging of the system around the Z axis. We set the Z axis of the molecular frame to be identical with the Z axis of the lab frame. Then the partial rotational averaging over (x, y) rotation leads to

$$\begin{aligned}\langle(\mathbf{a}\cdot\boldsymbol{\alpha})(\mathbf{b}\cdot\boldsymbol{\beta})(\mathbf{c}\cdot\boldsymbol{\gamma})(\mathbf{d}\cdot\boldsymbol{\eta})\rangle = {} & 2a_z b_z c_z d_z \alpha_z \beta_z \gamma_z \eta_z + \\ & \sum_{ijpq=x,y} (a_z b_z c_p d_q \alpha_z \beta_z \gamma_i \eta_j + a_z b_p c_z d_q \alpha_z \beta_i \gamma_z \eta_j + \\ & a_z b_p c_q d_z \alpha_z \beta_i \gamma_j \eta_z + a_p b_z c_z d_q \alpha_i \beta_z \gamma_z \eta_j + a_p b_z c_q d_z \alpha_i \beta_z \gamma_j \eta_z + \\ & a_p b_q c_z d_z \alpha_i \beta_j \gamma_z \eta_z)\langle ip, jq\rangle_{xy} + \\ & \sum_{pqrsijkl=x,y} a_p b_q c_r d_s \alpha_i \beta_j \gamma_k \eta_l \langle ip, jq, kr, ls\rangle_{xy}\end{aligned} \quad \text{(A1)}$$

where

$$\langle ip, jq\rangle_{xy} = \delta_{kr}\delta_{ls} + \delta_{kl}\delta_{rs} - \delta_{ks}\delta_{rl} \quad \text{(A2)}$$

and

$$\begin{aligned}\langle ip, jq, kr, ls\rangle_{xy} = {} & (3/4)\{\delta_{ip}\delta_{jq}\delta_{kr}\delta_{ls} + \zeta_{ip}\zeta_{jq}\zeta_{kr}\zeta_{ls} \times \\ & (\delta_{ij}\delta_{kl}\zeta_{jk} + \delta_{ik}\delta_{jl}\zeta_{ij} + \delta_{il}\delta_{jk}\zeta_{ij} - \delta_{ij}\delta_{jk}\zeta_{kl} - \delta_{ij}\delta_{jl}\zeta_{kl} - \\ & \delta_{ik}\delta_{kl}\zeta_{ij} - \delta_{jk}\delta_{kl}\zeta_{ij} + \delta_{ij}\delta_{jk}\delta_{kl})\} + (1/4)\{\delta_{ip}\delta_{jq}\delta_{kl}\delta_{rs}\zeta_{kr} + \\ & \delta_{ip}\delta_{kr}\delta_{jl}\delta_{qs}\zeta_{jq} + \delta_{ip}\delta_{ls}\delta_{kj}\delta_{rq}\zeta_{kr} + \delta_{kr}\delta_{jq}\delta_{il}\delta_{ps}\zeta_{ip} + \\ & \delta_{ls}\delta_{jq}\delta_{ki}\delta_{rp}\zeta_{kr} + \delta_{kr}\delta_{ls}\delta_{ij}\delta_{pq}\zeta_{ip} - \delta_{ip}\delta_{jq}\delta_{ks}\delta_{lr}\zeta_{kl} - \\ & \delta_{ip}\delta_{kr}\delta_{js}\delta_{lq}\zeta_{jl} - \delta_{ip}\delta_{ls}\delta_{kq}\delta_{jr}\zeta_{kj} - \delta_{kr}\delta_{jq}\delta_{is}\delta_{lp}\zeta_{il} - \\ & \delta_{ls}\delta_{jq}\delta_{kp}\delta_{ir}\zeta_{ki} - \delta_{kr}\delta_{ls}\delta_{iq}\delta_{jp}\zeta_{ij}\}\end{aligned} \quad \text{(A3)}$$

where $\zeta_{ij} = (1 - \delta_{ij})$ and the summation indices p, q, r, s and i, j, k, l take the values x and y.

References and Notes

(1) Stryer, L. *Biochemistry*, 2nd ed.; W. H. Freeman Company: New York, 1995

(2) Segel, D. J.; Bachmann, A.; Hofrichter, J.; Hodgson, K. O.; Doniach, S.; Kiefhaber, T. *J. Mol. Biol.* **1999**, *288*, 489.

(3) Arai, S.; Hirai, M. *Biophys. J.* **1999**, *76*, 2192.

(4) Balbach, J. *J. Am. Chem. Soc.* **2000**, *122*, 5887.

(5) Pfuhl, M.; Driscoll, P. C. *Philos. Trans. R. Soc. London, Ser. A* **2000**, *358*, 513.

(6) Wuthrich, K. *NMR of Proteins and Nucleic Acids*; Wiley-Interscience: New York, 1986.

(7) Domche, W., Hochstrasser, R. M., Trommsdorff, H., Eds. *Chem. Phys.* **2004**, Special issue—Ultrafast Science with X-rays and Electrons.

(8) Fasman, G. *Circular Dichroism and the Conformational Analysis of Biomolecules*; Plenum: New York, 1996.

(9) Parker, F. *Applications of Infrared, Raman, and Resonance Raman Spectroscopy*; Plenum: New York, 1983.

(10) Mantsch, H. H.; Chapman, D. *Infrared Spectroscopy of Biomolecules*; Wiley-Liss: Chichester, U.K., 1996.

(11) Havel, H. *Spectroscopic Methods for Determining Protein Structure in Solution*; VCH Publishers: NewYork, 1996.

(12) Creighton, T. E. *Proteins: Structures and Molecular Properties*; W. H. Freeman and Company: New York, 1997.

(13) Torii, H.; Tatsumi, T.; Kanazawa, T.; Tasumi, M. *J. Phys. Chem. B* **1998**, *102*, 309.

(14) Surewicz, W. K.; Mantsch, H. H.; Chapman, D. *Biochemistry* **1993**, *32*, 389.

(15) Jackson, M.; Mantsch, H. H. *Crit. Rev. Biochem. Mol. Biol.* **1995**, *30*, 95.

(16) Bredenbeck, J.; Helbing, J.; Behrendt, R.; Renner, C.; Moroder, L.; Wachtveitl, J.; Hamm, P. *J. Phys. Chem. B* **2003**, *107*, 8654.

(17) Woutersen, S.; Hamm, P. *J. Chem. Phys.* **2001**, *115*, 7737.

(18) Woutersen, S.; Pfister, R.; Hamm, P.; Mu, Y.; Kosov, D. S.; Stock, G. *J. Chem. Phys.* **2002**, *117*, 6833.

(19) Bredenbeck, J.; Helbing, J.; Sieg, A.; Schrader, T.; Zinth, W.; Renner, C.; Behrendt, R.; Moroder, L.; Wachtveitl, J.; Hamm, P. *Proc. Natl. Acad. Sci. U.S.A.* **2003**, *100*, 6452.

(20) Chi, Z.; Chen, X. G.; Holtz, J. S. W.; Asher, S. A. *Biochemistry* **1998**, *37*, 2854.

(21) Baumruk, V.; Pancoska, P.; Keiderling, T. A. *J. Mol. Biol.* **1996**, *259*, 774.

(22) Stephens, P. J.; Lowe, M. A. *Annu. Rev. Phys. Chem.* **1985**, *36*, 231.

(23) Mukamel, S. *Annu. Rev. Phys. Chem.* **2000**, *51*, 691.

(24) Mukamel, S.; Hochstrasser, R. M. *Chem. Phys.* **2001**, *266*, special issue on Multidimensional Spectroscopies.

(25) Nibbering, E. T. J.; Elsasser, T. *Chem. Rev.* **2004**, *104*, 1887.

(26) Hamm, P.; Hochstrasser, R. M. Structure and Dynamics of Proteins and Peptides: femtosecond two-dimensional spectroscopy. *Ultrafast Infrared and Raman Spectroscopy*; Marcel Dekker, Inc.: New York, 2001.

(27) Fang, C.; Wang, J.; Charnley, A. K.; Barber-Armstrong, W.; Smith, A. B.; Decatur, S. M.; Hochstrasser, R. M. *Chem. Phys. Lett.* **2003**, *382*, 586.

(28) Khalil, M.; Tokmakoff, A. *Chem. Phys.* **2001**, *266*, 213.

(29) Golonzka, O.; Khalil, M.; Demirdoven, N.; Tokmakoff, A. *Phys. Rev. Lett.* **2001**, *86*, 2154.

(30) Zhang, W. M.; Chernyak, V.; Mukamel, S. *J. Chem. Phys.* **1999**, *110*, 5011.

(31) Zanni, M. T.; Ge, N. H.; Kim, Y. S.; Hochstrasser, R. M. *Proc. Natl. Acad. Sci. U.S.A.* **2001**, *98*, 11265.

(32) Ge, N. H.; Zanni, M. T.; Hochstrasser, R. M. *J. Phys. Chem. A* **2002**, *106*, 962.

(33) Hamm, P.; Lim, M. H.; Hochstrasser, R. M. *J. Phys. Chem. B* **1998**, *102*, 6123.

(34) Hamm, P. *Chem. Phys.* **1995**, *200*, 415.

(35) Joo, T. H.; Jia, Y. W.; Yu, J. Y.; Jonas, D. M.; Fleming, G. R. *J. Phys. Chem.* **1996**, *100*, 2399.

(36) Jimenez, R.; vanMourik, F.; Yu, J. Y.; Fleming, G. R. *J. Phys. Chem. B* **1997**, *101*, 7350.

(37) Bruccoleri, R.; Karplus, M. *Biopolymers* **1987**, *26*, 137.

(38) Brunger, A.; Karplus, M. *Science* **1987**, *235*, 458.

(39) Weiner, S.; Kollman, P.; Case, D.; Singh, U.; Ghio, C.; Alagona, G.; Profeta, S.; Weiner, P. *J. Am. Chem. Soc.* **1984**, *106*, 765.

(40) Kirkpatrick, S.; Gelatt, C.; Vecchi, M. *Science* **1983**, *220*, 671.

(41) VanGunsteren, W. F. *Prog. Biophys. Mol. Biol.* **1996**, *65*, SA301.

(42) Brooks, C.; Onuchic, J.; Wales, D. *Science* **2001**, *293*, 612.

(43) Moran, A. M.; Park, S. M.; Mukamel, S. *J. Chem. Phys.* **2003**, *118*, 9971.

(44) Davydov, A. *Theory of Molecular Excitons*; McGraw-Hill: New York, 1962.

(45) Kuhn, T.; Schwalbe, H. *J. Am. Chem. Soc.* **2000**, *122*, 6169.

(46) Piryatinski, A.; Chernyak, V.; Mukamel, S. *Chem. Phys.* **2000**, *266*, 285.

(47) *MacroModel 8.5 User Manual*; Schrodinger Company: New York, 2003.

(48) Leach, A. *Molecular Modelling: Principles and Applications*; Addison Wesley Longman, Limited: Reading, MA, 1998.

(49) Luzar, A.; Chandler, D. *Nature* **1996**, *379*, 55.

(50) Moran, A.; Mukamel, S. *Proc. Natl. Acad. Sci. U.S.A.* **2004**, *101*, 506.

(51) Krimm, S.; Abe, Y. *Proc. Natl. Acad. Sci. U.S.A.* **1972**, *69*, 2792.

(52) Moore, W. H.; Krimm, S. *Proc. Natl. Acad. Sci. U.S.A.* **1975**, *72*, 4933.

(53) Krimm, S.; Bandekar, J. *Adv. Protein Chem.* **1986**, *38*, 181.

(54) Torii, H.; Tasumi, M. *J. Raman Spectrosc.* **1998**, *29*, 81.

(55) Mukamel, S. *Principles of Nonlinear Optical Spectroscopy*; Oxford University Press: New York, 1995.

(56) Mukamel, S.; Abramavicius, D. *Chem. Rev.* **2004**, *104*, 2073.

(57) Soreghan, B.; Pike, C.; Kayed, R.; Tian, W. Q.; Milton, S.; Cotman, C.; Glabe, C. G. *NeuroMol. Med.* **2002**, *1*, 81.

(58) Soreghan, B.; Kosmoski, J.; Glabe, C. *J. Biol. Chem.* **1994**, *269*, 28551.

(59) Cribbs, D. H.; Velazquez, P.; Soreghan, B.; Glabe, C. G.; Tenner, A. J. *Neuroreport* **1997**, *8*, 3457.

(60) Yong, W.; Lomakin, A.; Kirkitadze, M. D.; Teplow, D. B.; Chen, S. H.; Benedek, G. B. *Proc. Natl. Acad. Sci. U.S.A.* **2002**, *99*, 150.

(61) Walsh, D. M.; Lomakin, A.; Benedek, G. B.; Condron, M. M.; Teplow, D. B. *J. Biol. Chem.* **1997**, *272*, 22364.

(62) Chirgadze, Y. N.; Shestopalov, B. V.; Venyaminov, S. Y. *Biopolymers* **1973**, *12*, 1337.

(63) Jackson, M.; Haris, P. I.; Chapman, D. *J. Mol. Struct.* **1989**, *214*, 329.

(64) Byler, D. M.; Susi, H. *Biopolymers* **1986**, *25*, 469.

(65) Surewicz, W. K.; Mantsch, H. H. *Biochim. Biophys. Acta* **1988**, *952*, 115.

(66) Demirdoven, N.; Cheatum, C.; Chung, H.; Khalil, M.; Knoester, J.; Tokmakoff, A. *J. Am. Chem. Soc.* **2004**, *126*, 7981.

(67) Abramavicius, D.; van Grondelle, R.; Valkunas, L. *Phys. Chem. Chem. Phys.* **2004**, *6*, 3097.

(68) Andrews, D. L.; Thirumachandran, T. J. *Chem. Phys.* **1977**, *67*, 5026. Hochstrasser, R. M. *Chem. Phys.* **2001**, *266*, 273.